A method of Extracting Flat Field from Real Time Solar Observation Data

YaHui Jin[1,2] · Hui Liu[1] · KaiFan Ji[1] · ZhenYu Jin[1] ·
WeiJie Meng[1,2]

Abstract Existing methods for obtaining flat field rely on observed data collected under specific observation conditions to determine the flat field. However, the telescope pointing and the column-fixed pattern noise of the CMOS detector change during actual observations. These leads to the residual signals in real-time observation data after flat field correction, such as interference fringes and column-fixed pattern noise. In actual observations, the wind causes the telescope to wobble slightly, which leads to shifts in the observed data. In this paper, a method of extracting the flat field from the real-time solar observation data is proposed. Firstly, the average flat field obtained by multi-frame averaging is used as the initial value. A set of real-time observation data is input into the KLL method to calculate the correction amount for the average flat field. Secondly, the average flat field is corrected using the calculated correction amount to obtain the real flat field for the current observation conditions. To overcome the residual solar structures caused by atmospheric turbulence in the correction amount, real-time observation data are grouped to calculate the correction amounts. These residual solar structures are suppressed by averaging multiple groups, improving the accuracy of the correction amount. The test results from diffraction-limited and ground-based simulated data demonstrate that our method can effectively calculate the correction amount for the average flat field. The NVST He I 10830 Å/Hα data were also tested. High-resolution reconstruction confirms that the correction amount effectively corrects the average flat field to obtain the real flat field for the current observation conditions. Our method works for chromosphere and photosphere data.

Keywords: Flat field · Data processing · Chromosphere data · Photosphere data

1. Introduction

Flat field correction is an important part of astronomical observation data processing, especially in high-resolution ground-based solar observations, where the accuracy of the flat field directly affects the reconstruction results of observed data. Therefore, all large-aperture ground-based solar telescopes, such as the Swedish Solar Telescope (SST), Goode Solar Telescope (GST), New Vacuum Solar Telescope (NVST), and GREGO Solar Telescope (Yang, Cao, and Yurchyshyn 2022), have made improving the flat field quality an important task. The NVST is a new vacuum solar telescope with a 985 mm clear aperture (Liu, Xu, and Gu 2014). There are two main groups of instruments, the Multi-band High Resolution Imaging System (MHRIS) and the grating spectrometer system. The MHRIS includes broadband interference filter channel (TiO-band) and two narrowband Lyot filter channels (Hα, He I 10830 Å). The grating spectrometer system consists of the Multi-band Spectrograph (MBS) in visible lines and the High Dispersion Spectrometer (HDS) in near-infrared lines (Cai, Yang, and Xiang 2022). Some parameters of MHRIS are shown in Table 1.

✉ H. Liu
liuhui@ynao.ac.cn

[1]   Yunnan Observatories, Chinese Academy of Sciences, Kunming 650011, China

[2]   University of Chinese Academy of Sciences, Beijing 100049, China

Table 1. Some parameters of MHRIS.

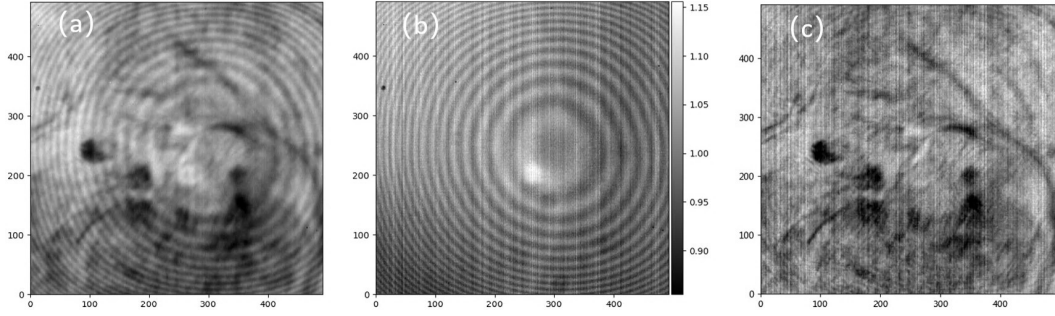| Channels	Filters	Bandpass(Å)	Focal length(m)	FOV
TiO	Interference Filter	10	35	$180'' \times 180''$
Hα	Lyot Filter	0.5	22.5	$168'' \times 168''$
10830 Å	Lyot Filter	0.25	20.58	$96'' \times 76''$

.

Figure 1. Panel (a) is NVST/He I 10830 Å observed data (the observed time is 13:42:37 UT on June 5, 2023), panel (b) is the average flat field (the observed time is 07:35:26 UT on June 5, 2023), and panel (c) is the high-resolution reconstructed data after correction of the average flat field. It can be easily seen that the high-resolution reconstructed data still contain residual signals after the average flat field correction, such as interference fringes, column-fixed pattern noise. The reconstruction method is non-rigid alignment (Liu et al. 2022)

Flat field obtaining methods can be divided into two categories: one is the multi-frame averaging method for small field of view (FOV) observations, which moves the telescope near the solar quiet region and then averages multiple images to obtain the flat field (called average flat field). This method is simple and has high accuracy. The root mean square (RMS) of pixel-to-pixel intensity variation in the flat field is about 0.1% (Moran, Foukal, and Rabin 1992; Yang et al. 2003). The other is the KLL method (Kuhn, Lin, and Loranz 1991) for large FOV observations, which was improved by Chae (2004). The KLL method records multiple images of solar disk with different parts of the detector by changing the telescope's pointing. The obtained images are used to calculate the flat field by iteration with some specific algorithm (Li et al. 2021). At present, it has been widely used in space or ground-based full-disk observations (Denker et al. 1999; Boerner et al. 2012; Fang et al. 2013). These methods all rely on a flat field observation pattern to move the telescope and obtain specialized flat field observed data to calculate the flat field. However, the observation conditions change during actual observations. In particular, the change in the telescope's pointing alters the relative angle between incident light and the detector's target surface, which in turn affects the intensity of interference fringes in the observed data. In addition, the column-fixed pattern noise of the CMOS detector changes over time (Wang et al. 2016; Qiu et al. 2021). Even with accurate flat fields, they don't reflect the current observation conditions, leading to residual signals like interference fringes and column-fixed pattern noise when applied to real-time observation data correction. These residual signals are further amplified in subsequent high-resolution reconstruction (Liu et al. 2021), as shown in Figure 1. Therefore, we need a method for obtaining flat field that can adapt to changes in observation conditions.

In small FOV ground-based solar observations, the slight wobble of the telescope caused by the wind leads to shifts in the observed data. We find that displacement characteristics of the observed data meet the requirements for extracting a flat field using the KLL method. Moreover, these observed data are obtained from real-time observations. Therefore, a set of real-time observation data can be input into the KLL method to extract the real flat field for the current observation conditions. However, extracting the real flat field directly from real-time observation data is very difficult. Since the average flat field is highly accurate, we regard real flat field of real-time observation data as the product of the average flat field and the correction amount. The average flat field is used as the initial value, and the correction amount for the average flat field is dynamically calculated from the real-time observation data using the KLL method. Finally, the calculated correction amount is used to correct the average flat field to obtain the real flat field for the current observation conditions.
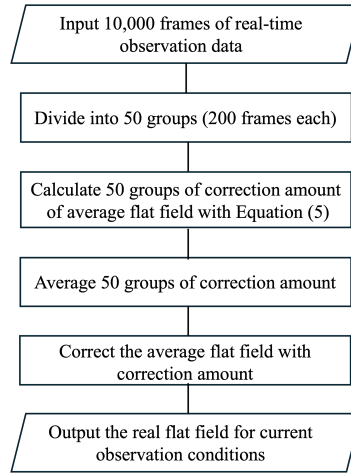
Figure 2. Flowchart of the overall algorithm.

The calculated correction amount may have residual significant solar structures, which will reduce the accuracy of the correction amount. This is because small FOV ground-based observed data are seriously distorted by atmospheric turbulence, which violates the KLL method's assumption that the solar intensity remains stable for a short time. Due to the random distortion of the observed data caused by atmospheric turbulence, the residual solar structures in the correction amount also exhibit random characteristics. Therefore, we can divide a large number of real-time observation data into multiple groups and use the KLL method to calculate the correction amount from each group. Finally, the correction amounts from multiple groups are averaged to suppress the residual solar structures, thereby improving the accuracy of the correction amount.

In this paper, a method of extracting flat field from real-time solar observation data is proposed. Firstly, a large number of real-time observation data are divided into multiple groups. Secondly, the average flat field is used as the initial value, and the correction amount for the average flat field is calculated from each group of real-time observation data using the KLL method. Thirdly, multiple groups of correction amount are averaged to suppress residual solar structures, thereby improving accuracy of the correction amount. Finally, the calculated correction amount is used to correct the average flat field to obtain real flat field for current observation conditions. Test results of diffraction-limited and ground-based simulated data demonstrate that our method can effectively calculates the correction amount for the average flat field. The NVST He I 10830 Å/Hα data were also used for testing. High-resolution reconstruction confirms that the calculated correction amount effectively corrects the average flat field to obtain the real flat field for current observation conditions.

The contents of this paper are organized as follows: In Section 2, the proposed method is introduced in detail. In Section 3, the diffraction-limited and ground-based simulated data are used to test the effectiveness of our method for calculating the average flat field correction amount. In Section 4, NVST He I 10830 Å/Hα observed data are also used to test the proposed method. In Sections 5, and 6 are discussed and summarized.

2. Method

The method proposed in this paper mainly includes four parts: (1) calculating the correction amount for the average flat field from real-time observation data using the KLL algorithm; (2) setting the initial value; (3) suppressing residual solar structures in the correction amount by group averaging; (4) correcting the average flat field by the calculated correction amount to obtain the real flat field for the current observation conditions.

2.1. Calculate the Correction Amount for the Average Flat Field

In small FOV ground-based solar observations, the slight wobble of the telescope caused by the wind. The solar observation object s is shifted by a vector a_i between two exposures.

$$s_i(x) = s\left(x - a_i\right) \tag{1}$$

where s_i denotes the incident signal on the detector. The vector x denotes a pixel in a coordinate frame fixed to the detector, and i denotes the ith frame in a series, $i = 1, 2, 3...N$. After removing the dark current and amplifier bias at each pixel, we have

$$obs_i(x) = s_i(x)f(x) \tag{2}$$

where obs_i denotes the the real-time observation data, and $f(x)$ is the pixel gain at x on the detector (commonly called the flat field).

In order to obtain the real flat field $f(x)$ of real-time solar observation data more accurately, we split $f(x)$ into the product of the average flat field and the correction amount, as shown in Equation (3).

$$f(x) = g_0(x)\Delta g(x) \tag{3}$$

where $g_0(x)$ is the average flat field, and $\Delta g(x)$ is the correction amount. We regard $g_0(x)$ as an initial value, which can be obtained by the multi-frame averaging method (Yang et al. 2003).

Substituting $f(x) = g_0(x) * \Delta g(x)$ into the Equation (2), the obs_i can be rewritten as

$$obs_i(x) = s_i(x)g_0(x)\Delta g(x) \tag{4}$$

We follow the optimization strategy improved by Chae (2004), where the solar observation object $s(x)$ is also used as the optimization target. The $s(x)$ and $\Delta g(x)$ can be solved using the least square method, as shown in Equation (5). We use the adaptive moment estimation (ADAM) optimization algorithm (Nair and Hinton 2015) to jointly solve for $s(x)$ and $\Delta g(x)$ in Equation (5).

$$(s(x)^*, \Delta g(x)^*) = \underset{(s(x), \Delta g(x))}{\mathrm{argmin}} \sum_{i=1}^{N} \left\| s_i(x)g_0(x)\Delta g(x) - obs_i(x) \right\|_2^2 \tag{5}$$

2.2. Set Initial Value

To accurately solve for the solar observation object $s(x)$ and the correction amount $\Delta g(x)$, we set initial values for $s(x)$ and $\Delta g(x)$. For setting the initial value of $s(x)$, it is very important to calculate the relative displacements of each real-time observation data. The calculation steps are as follows: Firstly, the average frame of the sequence real-time observation data is used as the reference; Secondly, the cross-correlation method is used to calculate the displacement vector a_i of each real-time observation data with respect to the reference, and the displacements need to be sub-pixel accurate; Finally, each real-time observation data is aligned to the reference, and the average frame after aligning the sequence real-time observation data is used as the initial value $s(x)^0$ of $s(x)$.

The above method can obtain $s(x)^0$ with a high signal-to-noise ratio, which helps to calculate $\Delta g(x)$ more accurately. However, there are a large number of high-frequency flat field signals in the real-time observation data, such as interference fringes, which will affect the accuracy of relative displacements calculation. We first preprocess the sequence of real-time observation data using the average flat field $g_0(x)$, and then calculate the relative displacements. The $g_0(x)$ can only process part of the flat field signals, but the preprocessed sequence real-time observation data is enough to calculate $s(x)^0$. The initial value of $\Delta g(x)$ is set to a matrix of ones.

The initial values of $s(x)$ and $\Delta g(x)$ are set as shown in Equation (6) - (7).

$$s(x)^0 = \frac{1}{N} \sum_{i}^{N} \mathrm{obs}_i(x)/g_0(x) \tag{6}$$
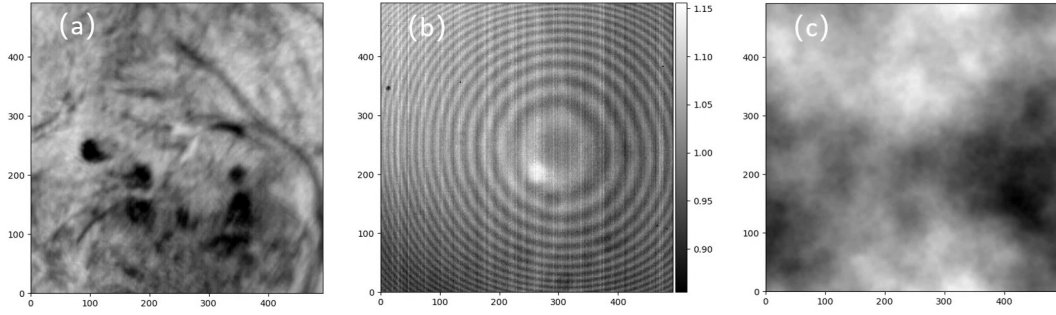
$$\Delta g(x)^0 = 1 \tag{7}$$

Figure 3. Panel (a) is the pre-processed NVST/He I 10830 Å observation data, which is used as the observation object (the observed time is 13:42:37 seconds on June 5, 2023), panel (b) is the average flat field (the observed time is 07:35:26 UT on June 5, 2023), which is used as the real flat field of the simulated data, and panel (c) is one of the randomly generated phase screens using the power spectrum inversion method (McGlamery 1967).

2.3. Suppress Residual Solar Structures in the Correction Amount

Although Equation (5) can calculate the correction amount for the average flat field from real-time observation data, significant solar structures remain in the correction amount. This is because the KLL method assumes that the solar intensity remains stable for a short time, but the small FOV ground-based observed data are severely distorted by atmospheric turbulence. This means that assumptions of the KLL method are violated.

Due to the random distortion of the ground-based observed data caused by atmospheric turbulence, the residual solar structures in the correction amount also exhibit random characteristics. Therefore, we can divide a large number of real-time observation data into multiple groups and then use the Equation (5) to calculate the correction amount $\Delta g(x)$ from each group of real-time observation data. Finally, multiple groups of correction amounts are averaged to suppress the residual solar structures, thus improving the accuracy of the correction amount. The average result of multiple groups of correction amounts is $\overline{\Delta g(x)}$.

In practical applications, a large amount of real-time observation data is divided into 50 groups (200 frames each) to calculate the correction amount for the average flat field.

We take 200 frames of real-time observation data as a group not only to calculate the correction amount but also to facilitate the subsequent high-resolution reconstruction process. There is no strict limit on the number of real-time observation data frames in each group, but the intensity between each frame of real-time observation data cannot differ too obviously. Otherwise, the correction amount for the average flat field cannot be calculated accurately.

Considering data processing efficiency, we chose to divide the large amount of real-time observation data into 50 groups. If more groups are added, signal-to-noise ratio of correction amount can be further improved.

2.4. Obtain the Real Flat Field for Current Observation Conditions

The correction amount $\overline{\Delta g(x)}$ for the average flat field calculated in Section 2.3 is used to correct the average flat field $g_0(x)$, so as to obtain the real flat field $\hat{f}(x)$ for the current observation conditions, as shown in Equation (8). The overall algorithm flowchart is shown in Figure 2.

$$\hat{f}(x) = g_0(x)\overline{\Delta g(x)} \tag{8}$$

3. Test with Simulated Data

In order to test the validity of our method in calculating the correction amount for the average flat field, we constructed two sets of simulated data: (1) The 200 frames of diffraction-limited simulated data are not affected by atmospheric turbulence. (2) The 100 groups of ground-based observed simulated data (200 frames each) are affected by atmospheric turbulence.

The simulated data (1) is constructed as follows: Firstly, a frame of flat dark field preprocessed NVST/He I 10830 Å observed data (the observed time is 13:42:37 UT on June 5, 2023) is used as the
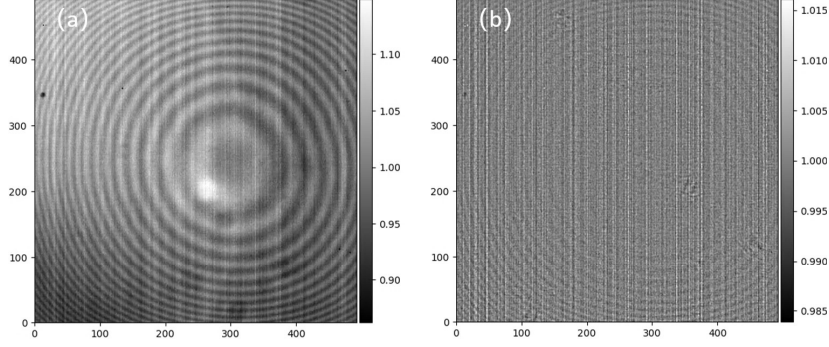
Figure 4. Panel (a) is the average flat field used for the calculation of the correction amount (observed time is 12:13:42 on June 4, 2023), and panel (b) is the true correction amount, which can be obtained by dividing the real flat field of the simulated data with the average flat field (panel (a)).
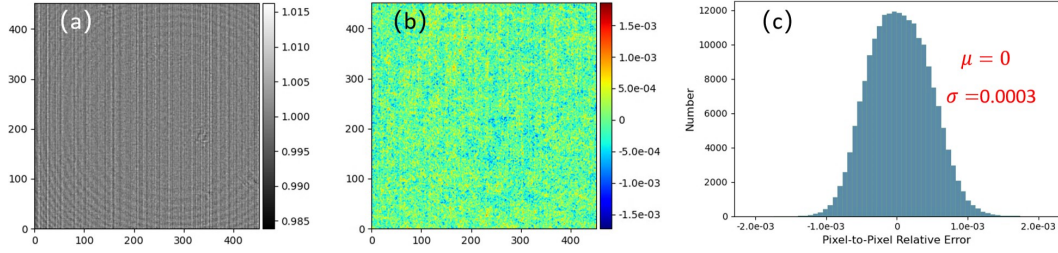

Figure 5. Visualization of correction amount calculated from diffraction-limited simulated data and its error analysis. Panel (a) is the correction amount calculated from the diffraction-limited simulated data, panel (b) is the pixel-to-pixel relative error of panel (a), and panel (c) is the error distribution histogram of panel (b).

solar observation object (Figure 3a). The average flat field (the observed time is 07:35:26 UT on June 5, 2023) is used as the real flat field (Figure 3b) of the diffraction-limited simulated data. Secondly, 200 groups of relative displacements (following a Gaussian distribution, ranging from 5 sub-pixels) are randomly generated to simulate the slight wobble of the telescope caused by the wind during actual observation. Finally, the displacements are integrated into the solar observation object (Figure 3a), and the displaced observation object is multiplied by the real flat field (Figure 3b) to generate 200 frames of diffraction-limited simulated data.

The simulated data (2) is constructed as follows: Firstly, the simulated data (2) and the simulated data (1) use the same solar observation object (Figure 3a) and the real flat field (Figure 3b). Secondly, 200 groups of relative displacements are generated in the same way as the simulated data (1), and the displacements are integrated into the solar observation object (Figure 3a). Thirdly, the displaced observation object is added to a random phase screen with the Fried parameter r_0 of 12 cm (Figure 3c), which simulates the distortion of ground-based observed data caused by atmospheric turbulence. Finally, the distorted data are multiplied by the real flat field (Figure 3b) to obtain one group (200 frames) of ground-based observed simulated data, and then the above steps are repeated to generate 100 groups of ground-based observed simulated data.

In this part, we use the simulated data to test the validity of our method in calculating the correction amount for the average flat field. The average flat field (observed time is 12:13:42 seconds on June 4, 2023) is shown in Figure 4a. Figure 4b shows the difference between the average flat field (Figure 4a) and the real flat field (Figure 3b) of the simulated data, which represents the true correction amount for the average flat field. Since we are using simulated data, the true correction amount is known. Therefore, we can evaluate the correction amount calculated by our method. The pixel-to-pixel relative error, w (its proportion reflects the accuracy), and the root mean square error (RMSE) are used as evaluation metrics, and the Equations are shown in (9)-(10).

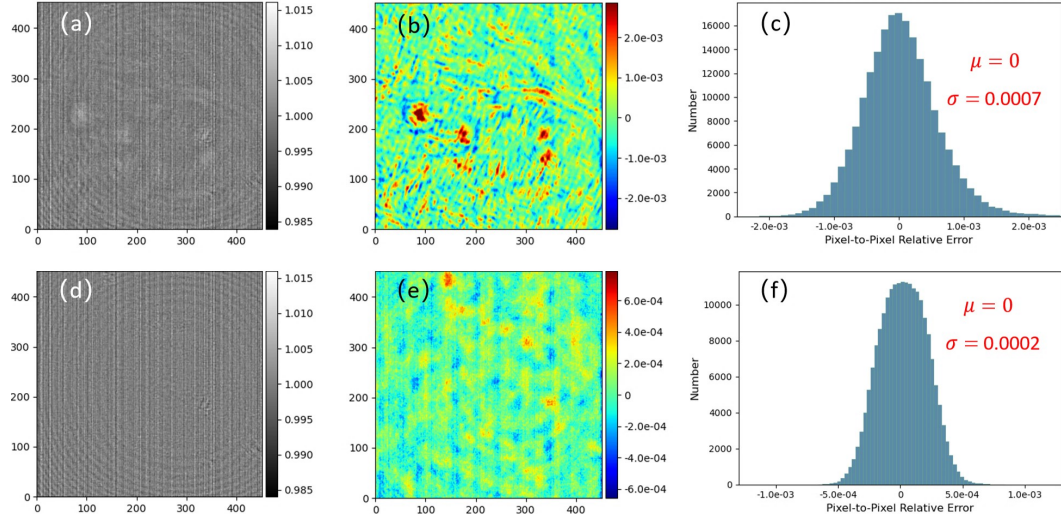$$w = \frac{F(x) - F_{\text{true}}(x)}{F_{\text{true}}(x)} \times 100\% \tag{9}$$

Figure 6. Visual comparison of correction amount calculation results from one group and 100 groups of ground-based observed simulated data and its error analysis. Panel (a)-(c) is the results for one group of ground-based simulated data, and panel (d)-(f) is the results for 100 groups of ground-based simulated data.

$$RMSE = \sqrt{\frac{1}{n}\sum_{i=1}^{n}\left(F(x_i) - F_{true}(x_i)\right)^2} \tag{10}$$

where $F(x)$ is the calculated correction amount, $F_{\text{true}}(x)$ is the actual correction amount, and n is the number of pixels.

Firstly, we use the diffraction-limited simulated data unaffected by atmospheric turbulence (200 frames) to calculate the correction amount for the average flat field. Figure 5a shows the results of the correction amount calculation, and there are no residual solar structures. Figure 5b shows the pixel-to-pixel relative error of Figure 5a. As can be seen from Figure 5b, the correction amount calculated by our method has no obvious errors from fringes or residual solar structures. Specifically, the proportion of $\mid w \mid < 0.1\%$ is about 98.52%, and the maximum of it is 0.18%. To visualize the error distribution of Figure 5b more intuitively, Figure 5c shows the histogram of the error distribution of Figure 5b. The mean value of the histogram is 0, and the standard deviation is 0.0003. This indicates that there is almost no systematic error in the calculation result of the correction amount, and the error only fluctuates within a very small range. This demonstrates that our method can efficiently calculate the correction amount for the average flat field from diffraction-limited simulated data.

Secondly, we use ground-based observed simulated data affected by atmospheric turbulence to calculate the correction amount for the average flat field. Figure 6 shows the correction amount calculated from one group and 100 groups of ground-based observed simulated data, and its pixel-to-pixel relative error. Figure 6a shows the correction amount calculated from one group (200 frames) of ground-based observed simulated data, and there are obvious residual solar structures. This is because the KLL method assumes that the solar intensity remains stable for a short time, but ground-based observed data is severely distorted by atmospheric turbulence. Figure 6b shows the pixel-to-pixel relative error of Figure 6a. It can be seen from Figure 6b, there is a relatively large error in the residual part of the solar structures. Specifically, the proportion of $\mid w \mid < 0.1\%$ is reduced to 85.70%, and the maximum error is up to 0.45%. Figure 6c shows the histogram of the error distribution of Figure 6b. The standard deviation is up to 0.0007, which is significantly higher than the diffraction-limited simulated data. This demonstrates that the residual solar structure caused by atmospheric turbulence reduces the accuracy of the correction amount.

In order to overcome the effects of atmospheric turbulence, we calculate 100 groups of correction amounts from 100 groups of ground-based observed simulated data. The 100 groups of correction amounts are then averaged to suppress the residual solar structures in the correction amount, thus improving the accuracy of the correction amount. Figure 6d shows the average results of 100 groups of correction amount, and it can be intuitively seen that the solar structures are suppressed. Figure 6e shows the pixel-to-pixel relative error of Figure 6d. Specifically, the proportion of $\mid w \mid < 0.1\%$ increases to 100%, and the maximum value reduces to 0.082%. Figure 6f shows the histogram of the error
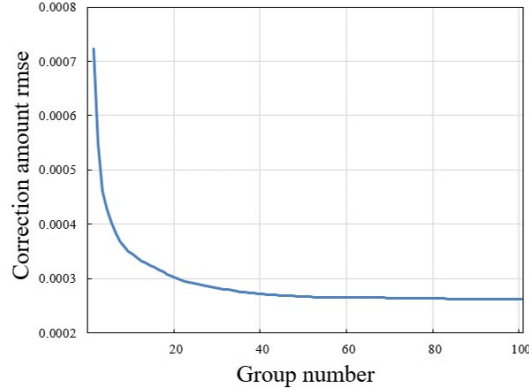
Figure 7. Root mean square error (RMSE) curve of correction amount calculated from different groups of ground-based observed simulated data.

distribution of Figure 6e. The standard deviation is only 0.0002, which is significantly lower than one group of ground-based simulated data. This demonstrates that the ground-based observation simulation data are grouped to calculate the correction amounts. Then, the results of multiple groups of correction amount are averaged, which can effectively suppress the residual solar structures in the correction amount, thereby improving the accuracy of the correction amount.

Figure 7 shows the RMSE curve for the correction amount calculated from different groups of ground-based observed simulated data. The RMSE reflects the overall error of the correction amount. As the number of groups of simulated data increases, the RMSE gradually decreases. The RMSE tends to converge when the number of groups reaches 50. This further demonstrates the effectiveness of grouped calculation and statistical averaging for determining the correction amount.

4. Test with NVST He I 10830 Å/Hα Observed Data

We use NVST He I 10830 Å/Hα observed data to test our method. The observation times of the two groups of data are 13:42:37 UT on June 5, 2023, and 02:53:42 UT on September 6, 2022, respectively. The He I 10830 Å observation data were recorded with 640×512 InGaAs CMOS camera, which was developed by the Astronomical Technology Laboratory of Yunnan Observatory in collaboration with the Kunming Institute of Physics in 2022 (Meng, Xu, and Jin 2023). Among them, the FOV covered by the He I 10830 Å channel observation data is $96'' \times 76''$, so the scale of each pixel is $0.15''$. The FOV covered by the Hα (6563 Å) channel observation data is $168'' \times 168''$ and recorded using a 2K × 2K CCD camera, so the ratio per pixel is $0.082''$. To improve the signal-to-noise ratio (SNR), the data is combined into 1k × 1k, so the scale of each pixel becomes $0.164''$ (Xiang, Liu, and Jin 2016).

We first use the average flat field obtained on the same day (observed time is 07:35:26 UT on June 5, 2023) as the initial value. Then, the correction amount for the average flat field is calculated from the NVST/He I 10830 Å observed data. Finally, the calculated correction amount is used to correct the average flat field to obtain the real flat field field for the current observation conditions.

Figure 8b shows the correction amount for the average flat field calculated by our method. It can be seen that there are obvious high-frequency signals in the correction amount, such as interference fringes and column-fixed pattern noise. The correction amount reflects the differences between the average flat field and the real flat field of the NVST/He I 10830 Å observed data. It is worth noting that these differences are unavoidable even if the average flat field accuracy is very high. The main reason is that the observed data used to calculate the average flat field are not obtained under actual observation conditions. Instead, we use the real-time observation data as input for the KLL method. The KLL method is then used to dynamically calculate the correction amount for the average flat field. Even if the observation conditions constantly change, we can correct the average flat field by the calculated correction amount so that the obtained flat field can adapt to the current observation conditions. Figure 8a shows the solar observed object calculated by our method, and it can be seen that the observed object has a high signal-to-noise ratio.

In order to verify the applicability of our method to the NVST/He I 10830 Å observed data, we processed the NVST/He I 10830 Å observed data with our method and the average flat field, respectively, and then reconstructed the processed results using a high-resolution reconstruction algorithm.
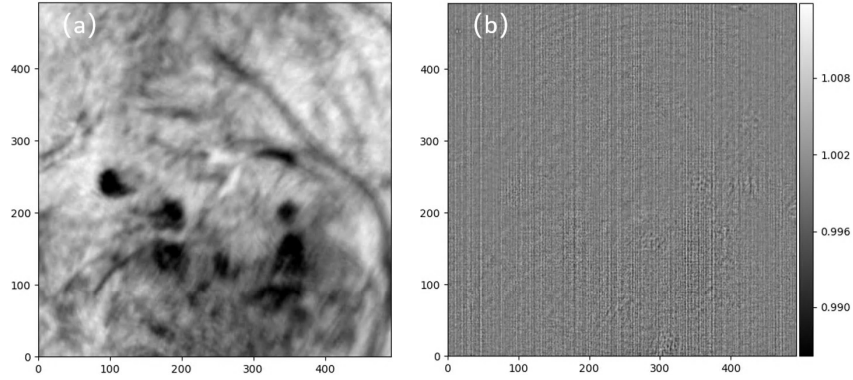
Figure 8. Panel (a) is the observation object calculated by our method from the NVST/He I 10830 Å data, and panel (b) is the correction amount for the average flat field calculated by our method.
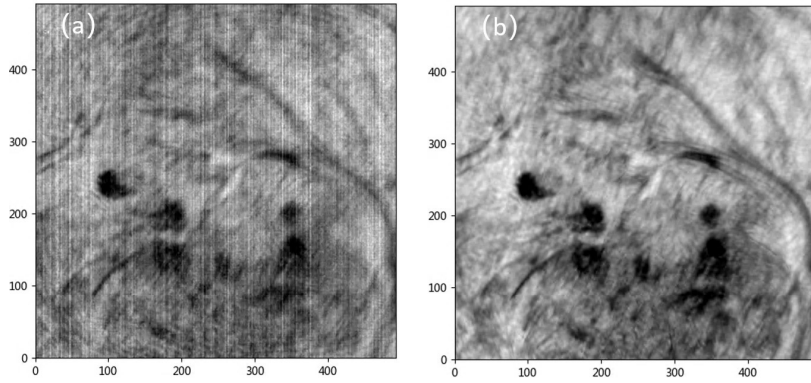

Figure 9. Comparison of high-resolution reconstructed data after processing NVST/He I 10830 Å data with different flat field correct methods. Panel (a) is the high-resolution reconstructed data after average flat field processing, and panel (b) is the high-resolution reconstructed data after processing by our method.

The reconstruction result is compared as shown in Figure 9. As can be seen from Figure 9a, when the observed data are processed by the average flat field, there are obvious residual signals in the high-resolution reconstruction results, such as interference fringes and column-fixed pattern noise. As shown in Figure 9b, when the observed data are processed using our method, it is difficult to see obvious residual signals in the high-resolution reconstruction result. This demonstrates that the correction amount calculated by our method can effectively correct the average flat field to obtain the real flat field for the current observation conditions, and provide accurate observation data for high-resolution reconstruction.

We also use NVST/Hα observation data to test the generalization capability of our method. Figure 10b shows the correction amount for the average flat field calculated from NVST/Hα observation data, and there are obvious interference fringes in the correction amount calculation result. Since the NVST/Hα observation data are obtained using a CCD camera, there is no significant column-fixed pattern noise in the correction amount. Figure 10a shows the observed object calculated by our method. Like the NVST/He I 10830 Å data, we processed the NVST/Hα observed data with our method and the average flat field, respectively, and then reconstructed the processed results using a high-resolution reconstruction algorithm. The reconstruction result is compared as shown in Figure 11. As shown in Figures 11c and d, when the observed data are processed by our method, it is difficult to see obvious residual signals in the high-resolution reconstruction result. In contrast, as shown in Figures 11a and b, when the observed data are processed by the average flat field, there are obvious residual signals in the high-resolution reconstruction result, such as interference fringes. This demonstrates that our method is also applicable to NVST/Hα observed data.
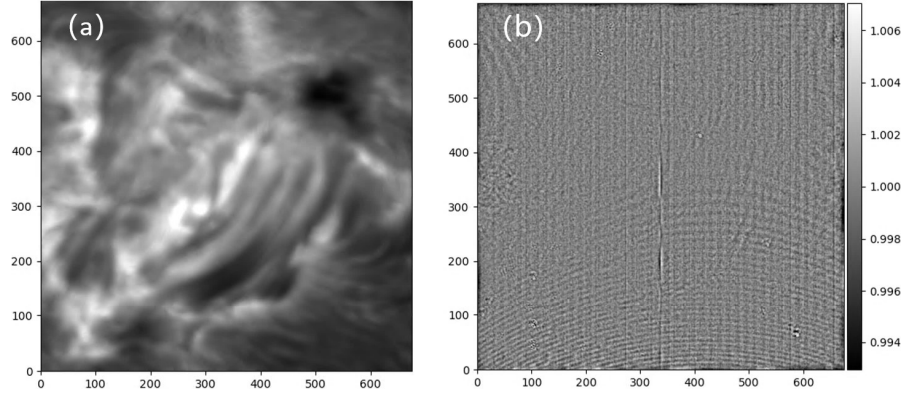
Figure 10. Panel (a) is the observed object calculated by our method from the NVST/Hα data, and panel (b) is the correction amount for the average flat field calculated by our method.
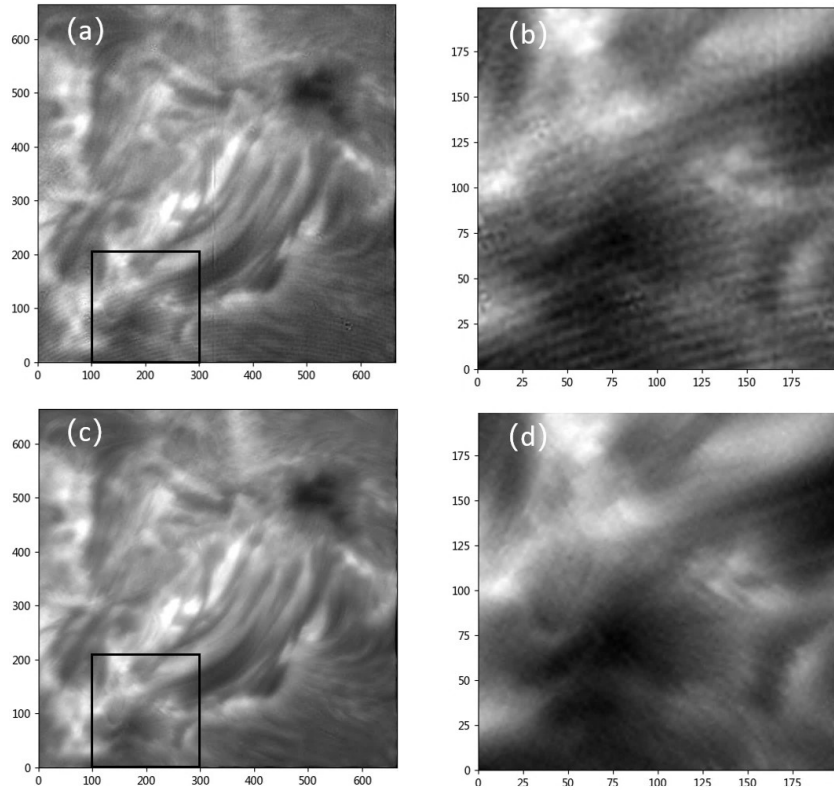

Figure 11. Comparison of high-resolution reconstructed data after processing NVST/Hα data with different flat field correct methods. Panel (a) is the high-resolution reconstructed data after average flat field processing, and panel (b) is the high-resolution reconstructed data after processing by our method, while panel (b) and (d) are the local regions of panel (a) and (c), respectively.

5. Discussion

The most direct purpose of our method is to obtain the real flat field for the current observation conditions, and improve the quality of subsequent high-resolution reconstruction. In actual observations, the observation conditions constantly change. It is necessary for the flat field obtaining method to adapt to the change of observation conditions. Some methods obtain a "fringe flat field" from observed data using multi-scale wavelet decomposition techniques (Zheng et al. 2016; Liu, Zheng, and Huang 2020; Liu et al. 2021) and manually set the model parameters for the current observation conditions, such as wavelet decomposition scale. When the observation conditions change, the model parameters must be readjusted. Even if these methods can manually adjust suitable model parameters and calculate the real flat field for the current observation conditions, it would be difficult to meet the real-time processing requirements of observed data, such as the need for immediate flat field correction.

Instead, we use an optimization approach to dynamically calculate the correction amount for the average flat field from real-time observation data. The calculated correction amount is then used to correct the average flat field to obtain the real flat field for the current observation conditions. The optimization algorithm can iteratively adjust the calculated correction amount to adapt to changes in the observation conditions. The overall calculation process does not need to rely on any preset parameters. Therefore, our method can effectively correct the observed data under various observation conditions and support the application of all-day observation. In addition, we use GPU to process the grouped real-time observation data, which accelerates the flat field calculation. It only takes about three minutes to obtain the real flat field for the current observation conditions. Therefore, our method has good applicability.

The displacement size of the real-time observation data is very important in calculating the correction amount for the average flat field. In actual observations, the displacement size of real-time observation data is small. And, these small shifted data can effectively capture high-frequency correction amounts, such as interference fringes and column-fixed pattern noise. In fact, these signals are the main factors affecting the quality of high-resolution data. We use the calculated high-frequency correction amount to correct the average flat field, which greatly reduces the residual signal in the observed data after flat field correction, thereby improving the high-resolution reconstruction results. Since the low-frequency flat field signal of the observed data is relatively stable in a short time, the average flat field as the initial value can process most of the low-frequency flat field signals.

6. Conclusion

In this paper, we propose a method of extracting the flat field from the real-time solar observation data, which can obtain the real flat field for the current observation conditions. In our method, a correction amount is calculated from real-time observation data using the optimization approach. Then, the calculated correction amount is used to correct the average flat field. Furthermore, a large number of real-time observation data are grouped to calculate correction amounts, and then multiple groups of correction amounts are averaged. This strategy overcomes the residual solar structures in the correction amount calculation results caused by atmospheric turbulence, further improving the accuracy of the correction amount. The test results of diffraction-limited and ground-based simulated data demonstrate that our method can effectively calculate the correction amount for the average flat field. The real NVST He I 10830 Å/Hα observation data confirm that the calculated correction amount effectively corrects the average flat field to obtain the real flat field for the current observation conditions. We want to highlight that the proposed method applies not only to chromosphere data but also to photosphere data.

However, it is difficult to capture the low-frequency correction amount using small displacement data. In the future, we can increase the telescope's wobble to introduce larger displacement, which will better capture the low-frequency correction amount and further improve the accuracy of the correction amount calculation.

References

Boerner, P., Edwards, C., Lemen, J., Rausch, A., Schrijver, C., Shine, R., Shing, L., Stern, R., Tarbell, T., Title, A., et al.: 2012, Initial calibration of the atmospheric imaging assembly (AIA) on the solar dynamics observatory (SDO). *The Solar Dynamics Observatory*, 41.

Cai, Y.F., Yang, X., Xiang, Y.Y.: 2022, The Co-alignment of Winged Hα Data Observed by the New Vacuum Solar Telescope. *Res. Astron. Astrophys* **22**, 289. DOI.

Chae, J.: 2004, Flat-fielding of solar Hα observations using relatively shifted images. *Solar Physics* **221**, 1.

Denker, C., Johannesson, A., Marquette, W., Goode, P., Wang, H., Zirin, H.: 1999, Synoptic hα full-disk observations of the sun from big bear solar observatory–i. instrumentation, image processing, data products, and first results. *Solar Physics* **184**, 87.

Fang, C., Chen, P.-F., Li, Z., Ding, M.-D., Dai, Y., Zhang, X.-Y., Mao, W.-J., Zhang, J.-P., Li, T., Liang, Y.-J., et al.: 2013, A new multi-wavelength solar telescope: Optical and Near-infrared Solar Eruption Tracer (ONSET). *Research in Astronomy and Astrophysics* **13**, 1509.

Kuhn, J.R., Lin, H., Loranz, D.: 1991, Gain calibrating nonuniform image-array data using only the image data. *PASP* **103**, 1097. DOI.

Li, J.-W., Li, H., Li, Y., Feng, L., Huang, Y., Zhao, J., Lu, L., Ying, B.-L., Xue, J.-C.: 2021, Methodology for in-flight flat-field calibration of the Lyman-alpha Solar Telescope (LST). *Research in Astronomy and Astrophysics* **21**, 121.

Liu, D.-J., Zheng, S., Huang, Y.: 2020, NVST chromosphere data interference fringes removal based on NSCT and PCA. *Astronomy and Computing* **30**, 100366.

Liu, D., Zheng, S., Huang, Y., Xiang, Y.: 2021, New Vacuum Solar Telescope Fringe Removal Based on "Fringes Flat Field". *SoPh* **296**, 28. DOI.

Liu, H., Jin, Z.Y., Xiang, Y.Y., Ji, K.F.: 2022, High-resolution solar image reconstruction based on non-rigid alignment. *Res. Astron. Astrophys* **22**, 278. DOI.

Liu, Z., Xu, J., Gu, B.Z.: 2014, New vacuum solar telescope and observations with high resolution. *Res. Astron. Astrophys* **14**, 705. DOI.

McGlamery, B.L.: 1967, Restoration of turbulence-degraded images. *JOSA* **57**, 293.

Meng, W.J., Xu, F.Y., Jin, Z.Y.: 2023, New Vacuum Solar Telescope Achieves Narrowband Infrared Solar Imaging Observation at He i 10830 Å. *Res. Astron. Astrophys* **24**, 513. DOI.

Moran, T., Foukal, P., Rabin, D.: 1992, A photometric study of faculae and sunspots between 1.2 and 1.6 μm. *Solar physics* **142**, 35.

Nair, V., Hinton, G.E.: 2015, Rectified linear units improve restricted boltzmann machines. In: *Proceedings of the International conference on learning representations (ICLR)*, 1520–1535. arXiv:1412.6980.

Qiu, P., Zhao, Y., Zheng, J., Wang, J.-F., Jiang, X.-J.: 2021, Research on performances of back-illuminated scientific CMOS for astronomical observations. *Res. Astron. Astrophys* **21**, 268.

Wang, S.B., Xu, Z., Xiang, Y.Y., JIN, Z.Y.: 2016, Analysis and elimination of interference fringes in the observation data of 1 m new vacuum solar telescope imaging system. *ACTA ASTRONOMICA SINICA* **57**, 608. DOI.

Xiang, Y.Y., Liu, Z., Jin, Z.Y.: 2016, High resolution reconstruction of solar prominence images observed by the New Vacuum Solar Telescope. *New Astronomy* **49**, 8. DOI.

Yang, G., Xu, Y., Wang, H., Denker, C.: 2003, High spatial resolution observations of pores and the formation of a rudimentary penumbra. *ApJ* **597**, 1190. DOI.

Yang, X., Cao, W., Yurchyshyn, V.: 2022, GST Data-processing Workflow: Image Registration and Alignment. *APJS* **262**, 55. DOI.

Zheng, S., He, S., Huang, Y., He, H.-L., Lin, G.-H.: 2016, Automated removal of stripe interference in full-disk solar images. *Research in Astronomy and Astrophysics* **16**, 002.